Cancer-associated metabolic alterations facilitated by astrocyte glycogenolysis mediate neuropathic pain chronicity

Junseo Park[1,2], Kwanghwan Kim[3], Hyewon Jun[3], Sung Joong Lee[4] *

[1]Department of Environmental Materials Science, College of Agriculture and Life Sciences, Seoul National University, Seoul, Republic of Korea.
[2]Department of Chemistry, College of Natural Sciences, Seoul National University, Seoul, Republic of Korea.
[3]Interdisciplinary Program in Neuroscience, College of Natural Science, Seoul National University, Seoul, Republic of Korea
[4]Department of Physiology and Neuroscience, Dental Research Institute, Seoul National University School of Dentistry, Seoul, Republic of Korea.

* Corresponding author

Abstract

Metabolic signal in astrocytes has been implicated in a range of neurophysiological disorders[1,2]. Likewise, pain chronification, defined by the transition from an acute to a persistent pain state in response to repeated or intense nociceptive stimuli, involves crucial contributions from astrocytes[3,4]. Although lactate transport by anterior cingulate cortex (ACC) astrocytes has been shown to influence pain chronification, the specific metabolic pathways and upstream signaling events remain poorly understood[4,5]. In this study, we identify glycogenolysis in ACC astrocytes as a central signaling mechanism controlling pain chronification. Inhibition of glycogenolysis suppressed pain-related behaviors and normalized neuronal hyperactivity. To further extend the glycogenolysis effects to the broader metabolic dynamics, we conducted integrated transcriptomic and metabolomic analyses as chronic pain progressed. Interestingly, these analyses revealed that chronic pain was accompanied by a shift toward cancer-associated metabolic programs in the ACC, which was driven by astrocytic glycogenolysis. Taken together, our findings demonstrated that pain chronification was mediated by astrocytic glycogenolysis, which induced cancer-associated metabolic pathway. This suggests that alterations in astrocytic glycogen metabolism could be key signals to cancer-associated metabolic reprogramming and these findings offer novel insights into astrocyte-driven oncogenic metabolic regulation in the neuropathic pathology.

Main

Neuropathic pain is a chronic pathological pain state arising from injury or dysfunction of the nervous system[3,6]. Repeated or intense nociceptive stimuli can drive the transition from acute to persistent pain[6,7]. This chronification is mediated by diverse adaptations within the central nervous system, including alterations in neuronal excitability and synaptic plasticity[3,7].

Glycogen metabolism is one of the well-established mechanisms underlying neuronal excitability and associated behaviors[8,9]. Notably, glycogen metabolism is primarily confined to astrocytes in the central nervous system, where its metabolites support and regulate neuronal excitability, particularly in response to traumatic stimuli[5,10,11]. By extension, dynamic shifts in astrocytic glycogen turnover may similarly contribute to the development of chronic pain. Indeed, modulation of glycogen dynamics in spinal cord astrocytes prevents the establishment of persistent pain, yet the role of astrocytic glycogen metabolism within supraspinal pain circuits remains unexplored[5,10]. Moreover, in the anterior cingulate cortex (ACC), inhibiting the transport of astrocyte-derived lactate—a product of glycogen metabolism—attenuated both pain chronification and neuronal hyperactivity[4,12,13]. However, it remains elusive how peripheral traumatic injury alters the dynamics of brain glycogen metabolism, thereby contributing to pain chronification.

Unlike non-transformed cells, cancer cells must simultaneously fulfill the demands for ATP generation, biosynthetic precursor supply, and reducing power to sustain their unchecked proliferation and growth[14]. To meet these requirements, tumor cells enact extensive metabolic reprogramming, remodeling pathways for glucose, amino acid, and lipid utilization; we defined cancer-associated metabolism[14,15]. Under hypoxic conditions, oncogenic transcription factors such as HIF-1α and c-Myc further enhance this adaptive flexibility by upregulating the expression of key metabolic enzymes[15].

A hallmark of this reprogramming is the Warburg effect, in which cancer cells convert the majority of imported glucose into lactate—even in the presence of ample oxygen[14,16]. This aerobic glycolysis enables rapid ATP production over short timescales and generates abundant intermediate metabolites that serve as building blocks for nucleotide, amino acid, and lipid synthesis[16]. Moreover, lactate accumulation acidifies the tumor microenvironment, thereby impairing effector immune cell function and fostering a pro-inflammatory milieu that can facilitate tumor progression[16].

Concomitantly, cancer cells exploit glutamine-driven glutaminolysis to replenish tricarboxylic acid (TCA) cycle intermediates via anaplerosis, sustaining continuous biosynthetic output[14,15,17]. By channeling glutamine into the TCA cycle, tumor cells not only maintain energy flux but also divert TCA intermediates into the synthesis of proteins, lipids, and antioxidants such as glutathione[17]. Together, these complementary pathways underpin the metabolic flexibility essential for tumor growth, survival, and metastatic potential[17].

Here, we demonstrated that astrocyte glycogen metabolism in ACC was reprogrammed during neuropathic pain chronification. Pharmacological blockade of glycogenolysis in the ACC rescued glycogen metabolism, neuronal hyperactivation, and pain chronification. Integrated transcriptomic and metabolomic profiling revealed an upregulation of cancer-associated metabolic pathways—akin to the Warburg effect—during the transition from acute to chronic pain, which was reversed upon glycogenolysis inhibition. These findings uncovered a novel astrocyte-centric metabolic mechanism driving chronic pain.

To investigate glycogen metabolic dynamics in the brain along with pain chronification, we harvested the ACC, a supraspinal hub for chronic pain processing[18], 1, 3, 5, and 7 days after spinal nerve transection (SNT). We induced neuropathic pain in mice by transecting the L5 spinal nerve[19,20,21], followed by performing a colorimetric glycogen assay (Fig. 1a). We confirmed that SNT mice developed chronic mechanical allodynia across days (Fig. 1b). Correspondingly, in the ACC contralateral to the injured nerve (contraACC), glycogen accumulated through day 1 to day 3 post-injury and then declined to the baseline by day 7 (Fig. 1c).

Glycogen is metabolized to lactate, a proposed chronic pain mediator[4], through glycogenolysis[10]. To investigate whether brain glycogenolysis contributes to pain chronification, we targeted the brain-specific glycogen phosphorylase isoform B (PYGB)[8,9]. We selected two chemically distinct PYGB inhibitors[22,23,24]—GPI-1 (5-Chloro-N-[(1S,2R)-2-hydroxy-3-(methoxymethylamino)-3-oxo-1-(phenylmethyl)propyl]-1H-indole-2-carboxamide) and GPI-2 (1-[3-(3-[2-Chloro-4,5-difluorobenzoyl]ureido)-4-methoxyphenyl]-3-methylurea)—and confirmed their appropriate binding interactions to PYGB using in silico docking analysis[25,26] (Extended Data Fig. 1a-d).

To test whether the PYGB inhibition influences pain chronification and a glycogenolytic product, we stereotaxically injected GPI-1 or GPI-2 directly into the contraACC of SNT mice, then conducted the von Frey test and nuclear magnetic resonance (NMR) spectroscopy (Fig. 1d). In both GPI-1 and GPI-2 treated groups, chronic mechanical allodynia was rescued across testing days (Fig. 1e), although they exhibited comparable acute mechanical sensitivity to the SNT control group (Fig. 1e). Seven days after SNT, we harvested the contraACC and performed NMR to quantify the glycogenolytic product glucose-1-phosphate (G1P). We found that G1P was significantly increased in SNT control mice, but was reversed by either PYGB inhibitor (Fig. 1f).

We further tested neuronal activation levels in the contraACC with immunohistochemical cell activation markers[4]: c-Fos, pCREB, and p-p38-MAPK. The number of c-Fos–positive neurons was elevated in SNT control mice relative to sham, but was significantly decreased following GPI-1 or GPI-2 treatment (Fig. 1g, h). Likewise, whereas both pCREB- and p-p38–positive neurons in the contraACC were enriched in the SNT mice, treatment with either GPI normalized their expression to sham levels (Extended Data Fig. 2a-d).

Given that ACC output to the nucleus accumbens (NAc) and ventral tegmental area (VTA) contributes to the affective behaviors under chronic pain[27,28], we examined c-Fos expression in these regions. In both NAc and VTA contralateral to injured nerve, SNT robustly induced neuronal activation, which was reversed by treatment of either GPI in the contraACC (Extended Data Fig. 3a-d). Together, these data demonstrate that blockade of glycogenolysis in the ACC following SNT injury attenuates not only local, but also circuit-wide neuronal hyperactivity.

In the central nervous system, glycogen metabolism is largely confined to astrocytes[8,9,10]. To further support and confirm this, we analyzed publicly available single-cell RNA sequencing data[29]. It revealed that the key glycogen metabolic enzyme transcripts[5,8,9,10], such as glycogen synthase 1(*Gys1*), *Pygb*, phosphorylase kinase regulatory subunit alpha 2 (*Phka2*) and protein phosphatase 1 regulatory subunit 3C (*Ppp1r3c*) are highly enriched in astrocyte clusters, with minimal expression in neurons or other glia (Fig. 2a, b).

We next asked whether the gene expression of glycogen metabolic enzymes in astrocytes changes over time in parallel with glycogen dynamics during pain chronification (Fig. 1c). To achieve astrocyte-specific mRNA profiling within defined time windows after SNT, we employed GFAP^{Cre}::RiboTag mice[30,31], with which we isolated translating mRNAs from the ACC and quantified *Gys1*, *Pygb*, *Phka2* and *Ppp1r3c* (Fig. 2c, Extended Data Fig. 4a-c). All four enzyme genes exhibited distinct temporal profiles during the transition from acute to chronic pain. Notably, *Ppp1r3c*—an activator of glycogenolysis—expression was highest when glycogen levels peaked, whereas *Pygb* expression reached its maximum by day 7 post-injury (Fig. 2d). These data indicate that the astrocytic glycogen machinery undergoes regulated during neuropathic pain chronification.

To directly assess the contribution of astrocytes to pain chronification, we selectively ablated ACC astrocytes by overexpressing caspase-3[32,33], followed by performing SNT surgery (Fig. 2e). We first confirmed astrocyte depletion in the contraACC by staining immunohistochemical astrocyte marker S100β (Fig. 2f). Ablation of astrocytes did not alter acute pain thresholds but elevated chronic pain thresholds by post-SNT; similar level of sham mice (Fig. 2g). We then quantified c-Fos positive neurons in the contraACC. Consistent with our PYGB inhibition results (Fig. 1g, h), astrocyte-ablated mice showed a significant reduction in c-Fos–expressing neurons compared to SNT controls (Fig. 2h–j). These findings demonstrate that ACC astrocytes are critical for the transition from acute to chronic pain, indicating the functional role of astrocyte glycogenolysis in pain chronification.

Glycogen breakdown is linked to the Warburg effect[9,16]. Accordingly, we quantified translating mRNAs associated with the Warberg effect using GFAP^{Cre}::RiboTag mice (Fig. 3a, Extended Data Fig. 4a-c). The hypoxia-inducible factor 1-a (*Hif-1a*), the lactate dehydrogenase a (*Ldha*) and b (*Ldhb*), and the monocarboxylate transporter 4 (*Mct4*) exhibited dynamic changes during pain chronification[14,15,16]. Notably, *Hif-1a* exhibited a prominent peak, *Ldha* and *Mct4* showed pronounced upregulation at the chronic pain time point (Fig. 3b).

In a parallel analysis, we examined transcriptomic profiles from the contraACC in the chronic constriction injury (CCI) model[34], which recapitulates features of SNT-induced neuropathic pain (Extended Data Fig. 5a). Seven days post-CCI, contraACC expression data were normalized against sham controls, and Gene Set Enrichment Analysis (GSEA) was performed for each pathway of interest[35] (Extended Data Fig. 4b–f). GSEA plots demonstrated significant upregulation of the Warburg effect and glutamate metabolism pathways under chronic pain conditions (Extended Data Fig. 5b, c). In contrast, aerobic glycolysis—opposed to the Warburg phenotype—as well as the tricarboxylic acid (TCA) cycle and oxidative phosphorylation (OXPHOS) pathways were all downregulated (Extended Data Fig. 5d–f). These results confirm that, at the transcriptomic level, cancer-associated metabolic programs such as the Warburg effect and glutamate metabolism are selectively reprogrammed during the chronic state of neuropathic pain.

As gene expression provides only indirect information about downstream metabolites[36,37,38], we next directly assessed metabolite fluxes by performing GC–MS–based metabolomics on ACC tissue collected at defined intervals following SNT (Fig. 3c). Individual metabolites displayed time-dependent dynamic profiles. Notably, several central carbon intermediates and amino acids progressively accumulated as pain transitioned from the acute to chronic state (Fig. 3d). To systematically evaluate these metabolic changes, we performed pathway enrichment analysis[37]. Over the course of pain chronification, Warburg effect and glutamate metabolism emerged as the most strongly enriched pathways (Fig. 3e–f). Moreover, multiple cancer-associated metabolic pathways were upregulated during the transition from acute to chronic pain (Fig. 3g).

To test how blockade of astrocytic glycogenolysis reshapes metabolic networks in the ACC, we stereotaxically injected GPI-1 or GPI-2 into the contraACC of SNT mice and performed 1H-NMR metabolomics at day 7 post-injury[39,40] (Fig. 4a). Metabolite concentrations were determined by NMR analysis and compared across groups (Fig. 4b-k, Extended Data. 6a-d).

In SNT controls, lactate was significantly increased relative to sham, whereas both GPI-1 and GPI-2 treatment restored lactate to baseline (Fig. 4b). We next examined key metabolites of tricarboxylic acid (TCA) cycle and glutamate metabolism. SNT animals

exhibited reduced succinate alongside increased pyruvate and malate compared to sham; PYGB inhibition reversed the latter two elevations, lowering pyruvate and malate toward sham values (Fig. 4c–e). Although glutamine and GABA showed no significant changes across groups, glutamate was markedly increased after SNT and significantly attenuated by GPI-1 or GPI-2 (Fig. 4f–h).

Focusing on the cancer-associated pathways highlighted by our GC-MS screen (Fig. 3), we performed pathway-level enrichment analysis for the Warburg effect and glutamate metabolism on the NMR data[37]. Both the enrichment p-value and expectation value for these pathways were substantially reduced in the PYGB-inhibited groups versus SNT controls (Fig. 4m–n). Furthermore, while SNT drove broad activation of multiple oncometabolic pathways, PYGB blockade substantially reduced both the impact scores and statistical significance of these pathways (Extended Data. 6e–h).

Collectively, these results demonstrated that astrocytic glycogenolysis in the ACC critically governed cancer-associated metabolic reprogramming—modulating lactate production, TCA cycle flux, and glutamate turnover—and that PYGB inhibition restored these maladaptive metabolic circuits while preventing pain chronification.

In summary, this study revealed that peripheral nerve injury modulated glycogen metabolism in the brain astrocyte, by which neuropathic pain was progressed as chronic. We found glycogenolysis in the ACC astrocyte is the key metabolic regulation for the neuropathic pain chronification. Within the ACC, glycogen metabolic dynamics emerge during the transition to chronic neuropathic pain, and astrocyte-derived glycogenolysis promotes pain chronification by enhancing neuronal excitability. Moreover, modulation of ACC astrocyte glycogenolysis controls cancer-associated metabolic alternation—particularly the Warburg effect and glutamate metabolism—thereby governing the chronification process. This finding represents the discovery of a novel glycogen-dependent astrocytic signaling mechanism that drives pain chronicity and provides the first elucidation of astrocyte-mediated pain chronification from the perspective of metabolic pathway dynamics.

Our transcription-metabolome analysis demonstrated that nerve injury-promoted astrocytic glycogen metabolism was closely associated with Warburg effect and other oncogenic metabolic alternation. This suggests cancer-inducing molecular dynamics change may cause a distinctive neurophysiological effect in the brain, thereby regulating pain and its related affective behaviors. Astrocyte metabolism has traditionally been viewed primarily as a means of regulating neuronal energy supply and neurotransmitter provision[41,42]. However, based on the alterations in cancer-associated metabolic programs revealed in this study, we propose that astrocytes can influence pathological processes not only by supplying metabolites to neurons but also through intrinsic shifts in their own metabolic flux. In particular, activation of cancer-associated metabolism implies a range of functional consequences. In classical cancer cells, oncogenic metabolic alternation drives not only activate in and support of metabolic pathways but also plays critical roles in immune evasion and the regulation of inflammatory responses. By analogy, in astrocytes such metabolic alternation may serve as a central mechanism for modulating diverse functions—including the activation of inflammatory pathways and the control of immune responses—via oncogenic-like metabolic shifts. We anticipate that such alterations in astrocytic metabolic dynamics will not only yield novel insights into the mechanisms underlying neurophysiological disorders but also highlight important targets for the development of new therapeutic strategies.

Methods

Animals

Animal experiments were approved by the Institutional Animal Care and Use Committee (IACUC) at Seoul National University. GFAP-Cre mouse and Rpl22$^{HA/HA}$ (RiboTag) were obtained from the Jackson Laboratory (GFAP-Cre: B6.Cg-Tg)Gfap-cre)77.6Mvs/2J, Rpl22$^{HA/HA}$: B6.129-Rpl22tm1.1Psam/J). We generated an astrocyte-specific RiboTag mouse by crossing floxed RiboTag mice with GFAP-Cre transgenic mice. The genotypes of mouse offspring were determined by PCR with the following primers:
GFAPcre-Fw: TCC ATA AAG GCC CTG ACA TC; *GFAPcre*-Rv: TGC GAA CCT CAT CAC TCG T; *RiboTag*-Fw: GGG AGG CTT GCT GGA TAT G; *RiboTag*-Rv: TTT CCA GAC ACA GGC TAA GTA CAC
Except for the RiboTag experiments, all mice used were C57BL/6. Male and female C57BL/6 mice (approximately 8 – 12 weeks of age) were purchased from DooYeol Biotech (Korea) and all animals were acclimatized to standard conditions with a 12-hr light/dark cycle in a specific pathogen-free environment and given access to chow and water ad libitum. All protocols were performed in accordance with the guidelines from the International Association for the Study of Pain.

Neuropathic pain mouse model

To generate a persistent pain model, the right L5 spinal nerve transection (SNT) was performed as previously described[43]. Briefly, animals were anesthetized with isoflurane in an O_2 carrier (induction 2% and maintenance 1.5%), and a small incision was made to expose the L4 and L5 spinal nerves. The L5 spinal nerve was transected.

Pain behavior test (von-Frey test)

Mechanical sensitivity of the right hind paw was assessed using a calibrated series of von Frey hairs (0.02–6 g, Stoelting, Wood Dale, IL, USA), following an up-down method[44]. Tests were performed after at least three habituations at 24-hr intervals. Assessments were made 1 day before surgery for baseline, and 1, 3, 5, and 7 days after injection. Rapid paw withdrawal, licking, and flinching were interpreted as a pain response. All behavioral tests were performed blinded.

Stereotaxic injection

For stereotaxic drug injection, C57BL/6 mice received unilateral injection of 1 μl GPI-1 (CP-316819, CAS 186392-43-8; TOCRIS, Minneapolis, MN, USA), GPI-2 (361515-1MG, CAS 648926-15-2; Sigma-Aldrich, St. Louis, MO, USA) in anterior cingulate cortex using coordinates AP: −1.0 mm, ML:0.4 mm, DV: −1.5 mm from the bregma. GPI-1 injected 500 nM, GPI-2 injected 300 nM. SNT surgery performed 1 h after drug injection.
For stereotaxic virus injection, C57BL/6 mice received unilateral injection of 1 μl pAAV-flex-a-taCasp3-TEVp, AAV-GFAP-Cre-WPRE-hGH, AAV5-gfaABC1D-tdTomato (~1×10^{13} gene copies (GC)/ml) in anterior cingulate cortex using coordinates AP: −0.9 mm, ML:0.4 mm, DV: −1.5 mm from the bregma. SNT surgery were performed 4 weeks after virus injection. The injection syringe (Hamilton, Reno, NV, USA) delivered GPI or AAV at a constant volume of 0.1 μl min^{-1} using a syringe pump (Stoelting, Wood Dale, IL, USA).

Immunohistochemistry

Mice were transcardially perfused with ice-cold 0.1 M phosphate-buffered saline (PBS; pH 7.4)

until all blood was removed, followed by perfusion with ice-cold 4% paraformaldehyde in 0.1 M PBS. Whole brains were post-fixed in 4% paraformaldehyde in 0.1 M PBS overnight at 4°C and cryoprotected with 30% sucrose for 3 days. Coronal 60 μm-thick sections were incubated in cryoprotectant at −20°C until immunohistochemical staining was performed. The sections were incubated in a blocking solution containing 5% normal Goat serum (Jackson ImmunoResearch, Bar Harbor, ME, USA), 2% BSA (Sigma-Aldrich), and 0.1% Triton X-100 (Sigma-Aldrich) for 1 h at room temperature.

Subsequently, the sections were incubated with mouse anti-NeuN (MAB377B, 1:1000; Millipore, Billerica, MA, USA), rabbit anti-S100β (ab52642, 1:500; Abcam, Cambridge, MA, USA), mouse anti-phospho-CREB (#9198 87G3, 1:1000; Cell Signaling Technology, Danvers, MA, USA) rabbit anti-p-p38 MAPK (# 9211S, 1:1000; Cell Signaling Technology) and rabbit anti-c-Fos (#2250 9F6, 1:1000; Cell Signaling Technology) antibodies overnight at 4°C in the blocking solution. After washing with 0.1 M PBS containing 0.1% Triton X-100, the sections were incubated for 1 h with FITC-, Cy3- or Cy5-conjugated secondary antibodies (1:200, Jackson ImmunoResearch) in the blocking solution at room temperature, washed three times, and then mounted on gelatin-coated glass slides using Vectashield (Vector Laboratories, Inc., Burlingame, CA, USA). Fluorescent images of the mounted sections were obtained using a confocal microscope (LSM800; Carl Zeiss, Jena, Germany).

Glycogen assay

Sample preparation

For brain sections, the animal was killed under isoflurane, and the brain was quickly released from the skull and immediately frozen with dry ice. Anterior cingulate cortex (ACC) sections were collected based on measurements from the Allen brain atlas and samples were snap-frozen and kept at −80°C until further processing.

Glycogen colorimetric assay

Tissue samples were homogenized in 200 μL of ddH_2O using a Dounce homogenizer on ice with 10–15 passes. Homogenates were boiled for 10 min to inactivate enzymes and subsequently centrifuged at 18,000 × g for 10 min at 4°C to remove insoluble material. The resulting supernatant was collected and used for glycogen analysis. To perform the assay, 2–50 μL of the tissue supernatant was added to a 96-well plate, and the volume was adjusted to 50 μL per well with glycogen hydrolysis buffer (provided in the Glycogen Colorimetric/Fluorometric Assay Kit (ab65620, Abcam)). For glycogen detection, 2 μL of hydrolysis enzyme mix was added to the wells designated for glycogen hydrolysis, while background control wells received no enzyme. Samples were incubated at room temperature for 30 min to allow hydrolysis of glycogen to glucose.

Following hydrolysis, 50 μL of a reaction mix containing 46 μL of development buffer, 2 μL of development enzyme mix, and 2 μL of OxiRed probe was added to all wells. Plates were incubated at room temperature for 30 min in the dark. Absorbance was measured at 570 nm using a microplate reader to quantify glycogen content. A standard curve was generated using glycogen standards (0–2 μg/well) prepared according to the manufacturer's instructions to determine sample glycogen concentrations. Background absorbance from control wells was subtracted from sample wells to account for any non-glycogen-derived signal. Glycogen concentration in each sample was normalized to the initial sample volume and adjusted based on dilution factors.

$$OD_{corrected} = OD_{sample} - OD_{background}$$

OD sample : Measured OD value for the sample well.
OD background : Measured OD value for the sample background control well. (Except hydrolysis mix – measure only background glucose constant)

$$Glycogen\ constant\ (\mu g/well) = \frac{OD_{corrected} - b}{m}$$

m : Slope of the standard curve (Glycogen constant).
b : Intercept of the standard curve.
OD corrected : Corrected OD value for the sample well.

Western Blot

For Western blotting, ACC tissues were homogenized in ice-cold RIPA buffer (50 mM Tris-HCl pH 7.5, 150 mM NaCl, 1% NP-40, 0.5% sodium deoxycholate, 0.1% SDS) supplemented with 1 mM PMSF and phosphatase inhibitor cocktail (Sigma-Aldrich, P5726). Homogenates were incubated on ice for 30 min, centrifuged at 13 000 rpm for 15 min at 4°C, and the supernatants collected. Protein concentration was measured by BCA assay (Pierce, 23225), and 20 µg of each sample was mixed with 5× SDS sample buffer, boiled for 5 min at 95°C, then resolved on 10% SDS-PAGE. Proteins were transferred to nitrocellulose membranes (LC2001; Invitrogen, Carlsbad, CA, USA) at 100 V for 1 h, blocked in 5% milk/TBST for 1 h, and probed overnight at 4°C with mouse anti-HA (ab9110, 1:2000; Abcam) and mouse anti-β-actin (A2228, 1:5000; Sigma-Aldrich) in 2.5% milk/TBST. After three TBST washes, membranes were incubated with HRP-conjugated goat anti-mouse IgG (1:3000 in 2.5% milk/TBST) for 1 h at room temperature. Blots were developed with SuperSignal™ West Pico PLUS (Thermo Fisher, Waltham, MA, USA) and imaged on a Fusion FX6.0 system; band intensities were quantified in ImageJ and normalized to β-actin.

qPCR

The real-time RT-PCR (qPCR) experiments were performed using the StepOnePlus Real-Time PCR system (Applied Biosystems, Foster City, CA, USA) following the $2^{-\Delta\Delta Ct}$ method. The total RNA from the contraACC tissue was extracted using TRIzol (Invitrogen) and reverse transcribed using TOPscript RT DryMIX (Enzynomics, Cat # RT200, Daejeon, Korea). All the ΔCt values were normalized to the corresponding GAPDH values and were represented as the fold change induction.

qPCR primers were used:

Ppp1r3c-Fw: GGT GAC TCA TCT TTC TGC CAC A; *Ppp1r3c*-Rv: CAA GAC AAA ATT AGG CAC GAG A; *Gys1*-Fw: ATC TAC ACT GTG CTG CAG ACG; *Gys1*-Rv: CCC TTG CTG TTC ATG GAA TCC; *Phka2*-Fw: TGG ATG CCA CCT CTC TCT TC; *Phka2*-Rv: TAT CTC CAC GCT CCC ACA TC; *Pygb*-Fw: CAG CAG CAT TAC TAT GAG CGG; *Pygb*-Rv: CCA AGT CCA ACC CCA ACT GA; *Hif-1a*-Fw: GAT CCT TGA TGC TTG CTG GG; *Hif-1a*-Rv: CTG TCC CCA ATG TCC AGA GT; *Ldha*-Fw: AAA GAG GAC TAA GGG GTG GC; *Ldha*-Rv: CTG CAG GAA ACA ACC ACT CC; *Ldhb*-Fw: AAA GGC TAC ACC AAC TGG GC; *Ldhb*-Rv: GCC GTA CAT TCC CTT CAC CA; *Mct4*-Fw: CAT TCC CAG GGA CGC AAA GAG; *Mct4*-Rv: GAC ACG GCT TGG ATC TCC TC

RNA-seq data analysis

Raw RNA-seq data were processed in Python to analyze relative gene expression between experimental and control groups. Raw counts were compared against the sham group and

normalized for library size using DESeq2's size-factor adjustment. A negative-binomial model was then fitted to calculate the $\log_2$ fold change and associated p-value for each gene. Genes were ranked in descending order by their $\log_2$FC/standard error, and Gene Set Enrichment Analysis (GSEA) was performed against the Hallmark and Gene Ontology gene sets. Normalized Enrichment Scores (NES) and false discovery rates (FDR) were computed, and enrichment plots were generated in GraphPad Prism. For each analysis, we selected gene sets corresponding to specific metabolic pathways to assess their degree of enrichment.

GC-MS

Tissue samples for GC–MS analysis were prepared from the ACC using the same dissection and freezing protocol as for the glycogen assay. For each contraACC specimen, 400 µL of tissue supernatant was collected and subjected to GC–MS. Derivatization was performed using trimethylsilylation (TMS), and 1 µL of each derivatized sample was injected onto a Thermo Scientific ISQ LT GC–MS system (Thermo Scientific, Waltham, MA, USA). Chromatographic separation and mass detection were carried out under standard operating conditions. Raw data were processed in Thermo Xcalibur Quan Browser: metabolites were identified by matching each chromatographic peak to reference spectra, and peak areas were integrated against baseline to obtain relative signal intensities. All metabolite abundances were then normalized to sham controls and expressed as fold changes for downstream analysis.

NMR

Tissue for NMR analysis of the ACC was prepared using the same dissection and freezing protocol as for the glycogen assay. For each contraACC sample, 500 µL of the tissue supernatant was collected and analyzed by NMR. Spectra were acquired on a Bruker AVANCE III HD 600 MHz high-resolution NMR spectrometer (Bruker BioSpin, Rheinstetten, Germany). Individual resonances were assigned using Chenomx NMR Suite Profiler, and metabolite concentrations were determined by integrating each peak relative to the subtraction baseline.

Metabolomics analysis

Absolute and relative metabolite concentrations obtained by GC–MS and NMR—including fold-change values normalized to sham controls—were subjected to comprehensive metabolomics analysis. For each metabolite, both absolute abundance and fold-change relative to the sham and saline + SNT groups were calculated, and statistical significance was assessed. To identify enriched metabolic pathways within each experimental group, we performed both Over-Representation Analysis (ORA) and Quantitative Enrichment Analysis (QEA). All pathway enrichment analyses were conducted using MetaboAnalyst v6.0. (http://www.metaboanalyst.ca).

Statistical analysis

The data were analyzed using GraphPad software. For comparisons between two groups, the Student's t-test was employed. For multiple group comparisons, two-way analysis of variance (ANOVA) was conducted, followed by Bonferroni's post hoc test. All data are expressed as the mean ± standard error of the mean (SEM), and statistical significance was defined as a p-value of < 0.05.

Reference

1. Theparambil, S.M., Kopach, O., Braga, A. *et al.* Adenosine signalling to astrocytes coordinates brain metabolism and function. *Nature* **632**, 139–146 (2024).
2. Ling, E., Nemesh, J., Goldman, M. *et al.* A concerted neuron–astrocyte program declines in ageing and schizophrenia. *Nature* **627**, 604–611 (2024).
3. Bliss, T. et al. Synaptic plasticity in the anterior cingulate cortex in acute and chronic pain. *Nat Rev Neurosci* **17**, 485–496 (2016).
4. Yin Wang. et al. Astrocyte-neuron lactate transport in the ACC contributes to the occurrence of long-lasting inflammatory pain in male mice. *Neurosci. Lett*, **764** (2021).
5. Marty-Lombardi, S., Lu, S., Ambroziak, W. *et al.* Neuron–astrocyte metabolic coupling facilitates spinal plasticity and maintenance of inflammatory pain. *Nat Metab.* **6**, 494–513 (2024).
6. Zhuo, M. Cortical excitation and chronic pain. *Trends Neurosci.* **31**, 199–207 (2008).
7. Zhuo, M. Long-term potentiation in the anterior cingulate cortex and chronic pain. *Phil. Trans. R. Soc. B* **369**, 20130146 (2014).
8. Markussen, K. H. et al. The multifaceted roles of the brain glycogen. *J. Neurochem.* **168**(5), 728–743 (2023)
9. Alberini CM. et al. Astrocyte glycogen and lactate: New insights into learning and memory mechanisms. *Glia*. 1244-1262 (2018).
10. Díaz-García, C.M. Glycogen from spinal astrocytes dials up the pain. *Nat Metab.* **6**, 384–386 (2024).
11. Magistretti, P. J. & Allaman, I. A Cellular Perspective on Brain Energy Metabolism and Functional Imaging. *Neuron*. **86**, 883–901 (2015).
12. Iqbal Z, Liu S, Lei Z, Ramkrishnan AS, Akter M, Li Y. Astrocyte L-Lactate Signaling in the ACC Regulates Visceral Pain Aversive Memory in Rats. *Cells.* **12**(1), 26 (2022).
13. Reid, P. et al. Astrocyte neuronal metabolic coupling in the anterior cingulate cortex of mice with inflammatory pain. *Brain Behav Immun,* **125**, 212–225 (2025).
14. Pavlova, N. N., & Thompson, C. B. (2016). The emerging hallmarks of cancer metabolism. *Cell Metabolism,* **23**(1), 27–47.
15. DeBerardinis, R. J., & Chandel, N. S. (2016). Fundamentals of cancer metabolism. *Science Advances,* **2**(5), e1600200.
16. Vander Heiden, M. G., Cantley, L. C., & Thompson, C. B. Understanding the Warburg effect: the metabolic requirements of cell proliferation. *Science,* **324**(5930), 1029–1033 (2009).
17. Altman, B. J., Stine, Z. E., & Dang, C. V. (2016). From Krebs to clinic: glutamine metabolism to cancer therapy. *Nature Reviews Cancer,* **16**(10), 619–634.
18. Guo, F., Du, Y., Qu, FH. et al. Dissecting the Neural Circuitry for Pain Modulation and Chronic Pain: Insights from Optogenetics. *Neurosci. Bull.* **38**, 440–452 (2022).
19. Lee J. *et al*. Ganglioside GT1b prevents selective spinal synapse removal following peripheral nerve injury. *EMBO Rep.* (2025)
20. Lee J, Hwang H, Lee SJ. Distinct roles of GT1b and CSF-1 in microglia activation in nerve injury-induced neuropathic pain. *Mol Pain*. **17** (2021)
21. Lim H. et al. GT1b functions as a novel endogenous agonist of toll-like receptor 2 inducing neuropathic pain. *EMBO J*. **39**(6) (2020)
22. Agathocleous, M., Love, N., Randlett, O. *et al.* Metabolic differentiation in the embryonic retina. *Nat Cell Biol* **14**, 859–864 (2012).
23. Xie, H., Song, J., Godfrey, J. *et al.* Glycogen metabolism is dispensable for tumour progression in clear cell renal cell carcinoma. *Nat Metab.* **3**, 327–336 (2021).

24. Ibrahim, M.M.H., Bheemanapally, K., Alhamami, H.N. *et al.* Effects of Intracerebroventricular Glycogen Phosphorylase Inhibitor CP-316,819 Infusion on Hypothalamic Glycogen Content and Metabolic Neuron AMPK Activity and Neurotransmitter Expression in Male Rat. *J Mol Neurosci.* **70**, 647–658 (2020).
25. W. -H. Shin, G. R. Lee, L. Heo, H. Lee, and C. Seok, Prediction of Protein Structure and Interaction by GALAXY protein modeling programs, *Bio Design*, **2**(1), 1-11 (2014).
26. J. Ko, H. Park, L. Heo, and C. Seok, GalaxyWEB server for protein structure prediction and refinement, *Nucleic Acids Res.* **40**(W1), W294-W297 (2012).
27. Song, Q., Wei, A., Xu, H. *et al*. An ACC–VTA–ACC positive- feedback loop mediates the persistence of neuropathic pain and emotional consequences. *Nat. Neurosci.* **27**, 272–285 (2024).
28. Gao SH. *et a*l. The projections from the anterior cingulate cortex to the nucleus accumbens and ventral tegmental area contribute to neuropathic pain-evoked aversion in rats. *Neurobiol Dis.* **140**, 104862 (2020).
29. Zhang et al. An RNA-sequencing transcriptome and splicing database of glia, neurons, and vascular cells of the cerebral cortex. *J Neurosci.* **34**(36), 11929-11947 (2014).
30. Boisvert MM, Erikson GA, Shokhirev MN, Allen NJ. The Aging Astrocyte Transcriptome from Multiple Regions of the Mouse Brain. *Cell Rep*. **22**(1), 269-285 (2018).
31. assoni, A., Farkhondeh, V., Itoh, Y. *et al.* The astrocyte transcriptome in EAE optic neuritis shows complement activation and reveals a sex difference in astrocytic C3 expression. *Sci Rep* **9**, 10010 (2019).
32. Yang CF. *et al*. Sexually dimorphic neurons in the ventromedial hypothalamus govern mating in both sexes and aggression in males. *Cell*. **9**;153(4):896-909 (2013).
33. Chan, K., Jang, M., Yoo, B. *et al.* Engineered AAVs for efficient noninvasive gene delivery to the central and peripheral nervous systems. *Nat Neurosci* **20**, 1172–1179 (2017).
34. Zhang, Y. *et al*. A transcriptomic analysis of neuropathic pain in the anterior cingulate cortex after nerve injury. *Bioengineered*, **13**(2), 2058–2075 (2022).
35. Li, J., Huang, K., Thakur, M. *et al.* Oncogenic TFE3 fusions drive OXPHOS and confer metabolic vulnerabilities in translocation renal cell carcinoma. *Nat Metab.* **7**, 478–492 (2025).
36. Gonzalez-Riano, C., Garcia, A. & Barbas, C. Metabolomics studies in brain tissue: a review. *J. Pharm. Biomed. Anal.* **130**, 141–168 (2016).
37. Xia, J., Wishart, D. Web-based inference of biological patterns, functions and pathways from metabolomic data using MetaboAnalyst. *Nat Protoc* **6**, 743–760 (2011).
38. Chan, E., Pasikanti, K. & Nicholson, J. Global urinary metabolic profiling procedures using gas chromatography–mass spectrometry. *Nat Protoc* **6**, 1483–1499 (2011).
39. Crook, A. A. & Powers, R. Quantitative NMR-Based Biomedical Metabolomics: current status and applications. *Molecules.* **25**, 1-33 (2020).
40. Pudełko-Malik, N., Drulis-Fajdasz, D., Pruss, Ł. *et al.* A single dose of glycogen phosphorylase inhibitor improves cognitive functions of aged mice and affects the concentrations of metabolites in the brain. *Sci Rep* **14**, 24123 (2024).
41. T. Matsui. *et al*., Astrocytic glycogen-derived lactate fuels the brain during exhaustive exercise to maintain endurance capacity, *Proc. Natl. Acad. Sci. U.S.A.* **114** (24) 6358-6363 (2017).
42. Natsubori A, *et al*. Serotonergic neurons control cortical neuronal intracellular energy dynamics by modulating astrocyte-neuron lactate shuttle. *iScience*. **5** 26(1), 105830 (2023).
43. Tanga FY, Nutile-McMenemy N, DeLeo JA. The CNS role of Toll-like receptor 4 in innate neuroimmunity and painful neuropathy. *Proc Natl Acad Sci U.S.A*. **102**(16) 5856-61 (2005).
44. Chaplan SR, Bach FW, Pogrel JW, Chung JM, Yaksh TL. Quantitative assessment of tactile

allodynia in the rat paw. *J Neurosci Methods*. **53**(1) 55-63 (1994).

Acknowledgement

This research was supported by 2024 Seoul National University undergraduate independent research in Student-Directed Education (SDE) program, and National Research Foundation of Korea (RS-2024-00402116).

Author contributions

J.S.P. designed the research, performed most experiments, analysed the data and wrote the first draft of the paper. K.H.K. contributed to data interpretation and manuscript revision. H.W.J. crossed RiboTag and GFAP-Cre mice to created astrocyte-specific RiboTag mice and assisted with experimental procedures. S.J.L. supervised the project.

Figure 1. ACC glycogenolysis mediate neuropathic pain chronification.
a, Experimental scheme of glycogen assay after neuropathic pain model surgery. **b**, von-Frey test of neuropathic pain model. Saline + Sham (black, n = 4), Saline + SNT (red, n = 9) mice, measured at baseline (BL) and days 1, 3, 7 post-surgery. ****$P < 0.0001$ (D3 SNT verses D3 Sham), ****$P < 0.0001$ (D7 SNT verses D7 Sham) **c**, Glycogen constant in ACC, compare by contralateral area and ipsilateral area. (Time point: Sham, D0.5, D1, D3, D7) ****$P < 0.0001$ (D1 SNT contra verses ipsi), ***$P = 0.0006$ (D3 SNT contra verses ipsi). **d**, Experimental scheme of NMR and IHC after GPI-1 stereotaxic injection in ACC. **e**, von-Frey test of neuropathic pain model. Saline + Sham (grey, n = 5), Saline + SNT (black, n = 10), GPI-1 + SNT (red, n = 10), GPI-2 + SNT (orange, n = 10) mice, measured at baseline (BL) and days 1, 3, 5, 7 post-surgery. **$P = 0.0035$ (D3 GPI-1 + SNT verses Saline + SNT), **$P = 0.0018$ (D3 GPI-2 + SNT verses Saline + SNT), ****$P < 0.0001$ (D5, D7 GPI-1 + SNT, GPI-2 + SNT verses Saline + SNT) **f**, NMR analysis of G1P constant in ACC contra area. (Saline + SNT: n = 4, Saline + Sham: n = 3, GPI-1 + SNT: n = 4, GPI-2 + SNT: n = 4). **$P = 0.0020$ (GPI-1 + SNT verse Saline + SNT), ***$P = 0.0010$ GPI-2 + SNT verse Saline + SNT) **g**, Representative confocal images of ACC. (Scale bar, 200 μm) **h**, IHC data of c-Fos+/NeuN+ cell in ACC. (Left): Number of c-Fos+/NeuN+ cell in ACC contra area. **$P = 0.0062$ (Saline + Sham verses Saline + SNT), ****$P < 0.0001$ (GPI-1 + SNT and GPI-2 + SNT verse Saline + SNT), (Right): Ratio of c-Fos+/NeuN+ cell in ACC contra area, compare with ipsi area. **$P = 0.0029$ (Saline + Sham verses Saline + SNT), ****$P < 0.0001$ (GPI-1 + SNT and GPI-2 + SNT verse Saline + SNT). Data are represented as the mean ± SEM; two-way ANOVA and t-test.

Figure 2. Astrocyte-specific mechanism underlie altered glycogen dynamics and pain chronification.

a, Scheme of glycogen metabolism pathway. (Created with https://www.biorender.com) **b**, Glycogen metabolism gene (*Ppp1r3c, Gys1, Phka2, Pygb*) single cell RNA-sequencing expression result of each cell type. **c**, Schematic illustration of GFAP^{Cre}::RiboTag mice and neuropathic pain model transcriptomics experiment. **d**, qPCR data of glycogen metabolism gene (*Ppp1r3c, Gys1, Phka2, Pygb*) fold change. (Time point: day1, day3 and day7; n = 6) **e**, Experimental Scheme of IHC after AAV-Caspase3 virus injection and SNT surgery. **f**, Representative confocal images of ACC of anti-s100b staining. **g**, von-Frey test of neuropathic pain model. tdTomato + Sham (grey, n = 5), tdTomato + SNT (black, n = 8), Casp3 + SNT (blue, n = 12) mice, measured at baseline (BL) and days 1, 3, 5, 7, 10, 14 post-surgery. ***P = 0.0010 (D5 Casp3 + SNT verses tdTomato + SNT), ****P < 0.0001 (D7, D10 and D14 Casp3 + SNT verses tdTomato + SNT) **h**, Representative confocal images of ACC. (Scale bar, 200 μm) **i-j**, IHC data of c-Fos+/NeuN+ cell in ACC. **i**, tdTomato or Caspase3 injection group analysis. (Left): Number of c-Fos+/NeuN+ cell in ACC contra area. ****P < 0.0001 (tdTomato + Sham and Casp3 + SNT verses tdTomato + SNT), (Right): Ratio of c-Fos+/NeuN+ cell in ACC contra area, compare with ipsi area. *P = 0.0062 (tdTomato + Sham verses tdTomato + SNT), ****P < 0.0001 (Casp3 + SNT verses tdTomato + SNT) **j**, Compare IHC data with GPI injection experiment. (Left): Number of c-Fos+/NeuN+ cell in ACC contra area. (no significant differences) (Right): Ratio of c-Fos+/NeuN+ cell in ACC contra area, compare with ipsi area. (no significant differences); Data are represented as the mean ± SEM; two-way ANOVA-multiple comparisons and t-value test.

589 **Figure 3. Identification of ACC metabolic dynamics during neuropathic pain**
590 **chronification.**
591 **a**, Schematic illustration of GFAP^{Cre}::RiboTag mice and neuropathic pain model
592 transcriptomics experiment. **b**, qPCR data of warburg effect gene (*Hif-1a, Ldha, Ldhb, Mct4;*
593 n = 6) fold change. (Time point: day1, day3 and day7, each time point: n = 6) **c**, Experimental
594 scheme of GC-MS metabolomics analysis in SNT pain model. **d**, Heatmap of metabolite fold-
595 changes relative to Sham at 12 h, D1, D3, D7 (n = 3 per time point). Data log_2-transformed and
596 Z-score normalized. **e-f**, Pathway enrichment analysis of GC-MS metabolomics data. Labeling
597 selected high enrichment metabolic pathway. **e**, 12h after SNT. **f**, 7d after SNT. **g**, Analysis of
598 the time-dependent enrichment of selected cancer-associated pathways. (Time point: 12h, 1d,
599 3d and 7d) Data are represented as the mean ± SEM. Pathway enrichment analysis of GC-MS
600 data is performed using MetaboAnalyst v6.0. (http://www.metaboanalyst.ca).
601

Figure 4. ACC glycogenolysis mediates cancer-assaociated metabolic changes in neuropathic pain chronification.

a, Experimental scheme of NMR metabolomics analysis in SNT pain model. **b-k**, Metabolite concentration data by NMR analysis. (Saline + SNT: n = 4, Saline + Sham: n = 3, GPI-1 + SNT: n = 4, GPI-2 + SNT: n = 4) **b**, Lactate concentration of each group. $^{**}P = 0.0084$ (Saline + Sham verse Saline + SNT), $^{*}P = 0.0141$ (GPI-1 + SNT verse Saline + SNT), $^{**}P = 0.0010$ (GPI-2 + SNT verse Saline + SNT) **c**, Pyruvate concentration of each group. $^{****}P < 0.0001$ (Saline + Sham verse Saline + SNT), $^{****}P < 0.0001$ (GPI-2 + SNT verse Saline + SNT) **d**, Succinate concentration of each group. $^{****}P < 0.0001$ (Saline + Sham verse Saline + SNT), $^{**}P = 0.0046$ (GPI-1 + SNT verse Saline + SNT), $^{**}P = 0.0010$ (GPI-2 + SNT verse Saline + SNT) **e**, Malate concentration of each group. $^{**}P = 0.0065$ (GPI-1 + SNT verse Saline + SNT), $^{***}P = 0.0001$ (GPI-2 + SNT verse Saline + SNT) **f**, Glutamate concentration of each group. $^{**}P = 0.0056$ (Saline + Sham verse Saline + SNT), $^{****}P < 0.0001$ (GPI-2 + SNT verse Saline + SNT) **g**, Glutamine concentration of each group. $^{*}P = 0.0240$ (GPI-2 + SNT verse Saline + SNT) **h**, GABA concentration of each group. (no significant differences) **i**, Alanine concentration of each group. $^{*}P = 0.0443$ (Saline + Sham verse Saline + SNT), $^{**}P = 0.0044$ (GPI-2 + SNT verse Saline + SNT) **j**, Arginine concentration of each group. $^{***}P = 0.0009$ (Saline + Sham verse Saline + SNT) **k**, Taurine concentration of each group. $^{*}P = 0.0282$ (Saline + Sham verse Saline + SNT), $^{**}P = 0.0024$ (GPI-2 + SNT verse Saline + SNT) **l**, Scheme of metabolic pathway of selected metabolism. **m-n**, Pathway enrichment analysis compare. **m**, Warburg effect pathway. **n**, Glutamate metabolism pathway. Data are represented as the mean ± SEM; t-value test. Pathway enrichment analysis of NMR data is performed using MetaboAnalyst v6.0. (http://www.metaboanalyst.ca).

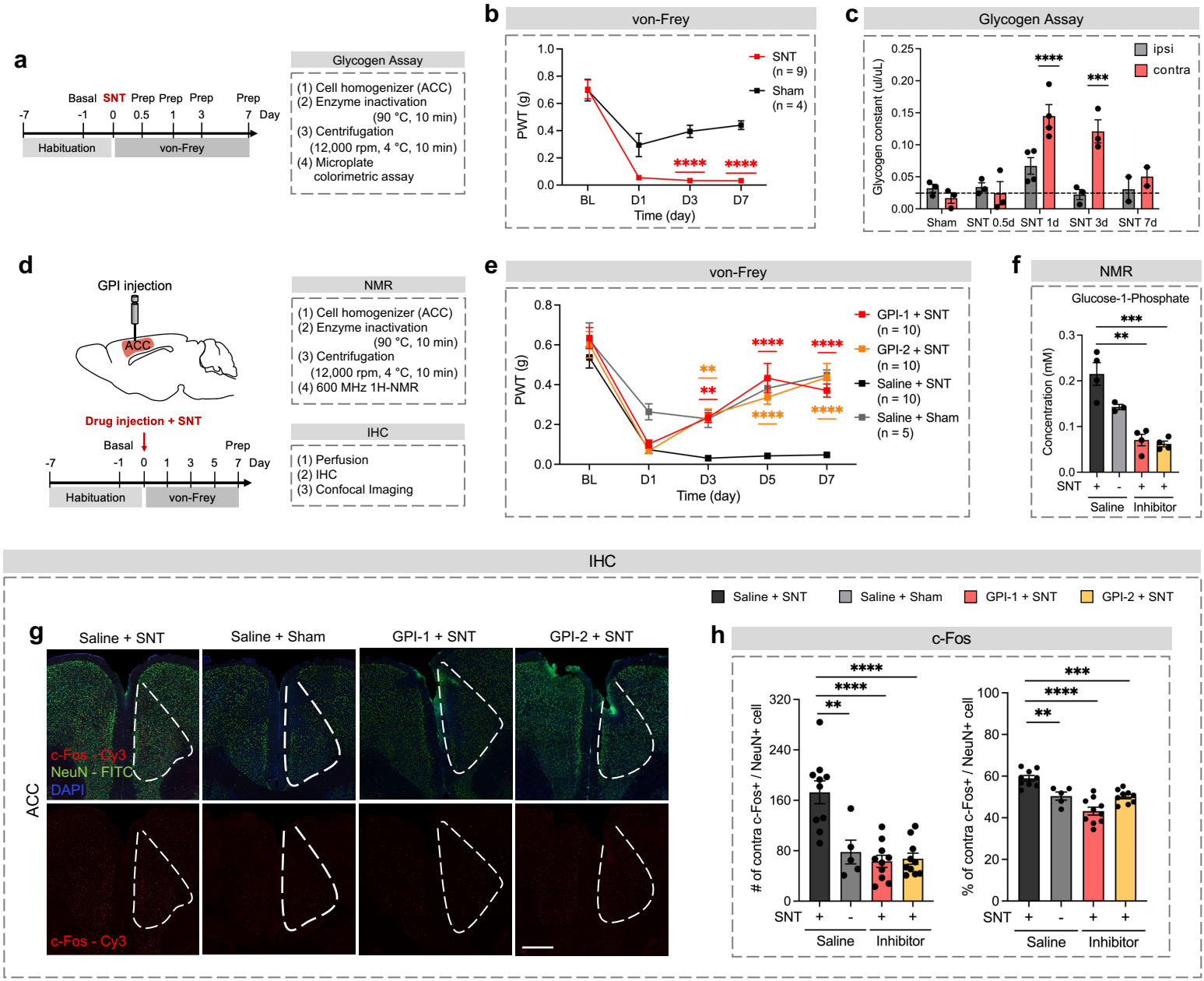

Figure 1. ACC glycogenolysis mediates neuropathic pain chronification.

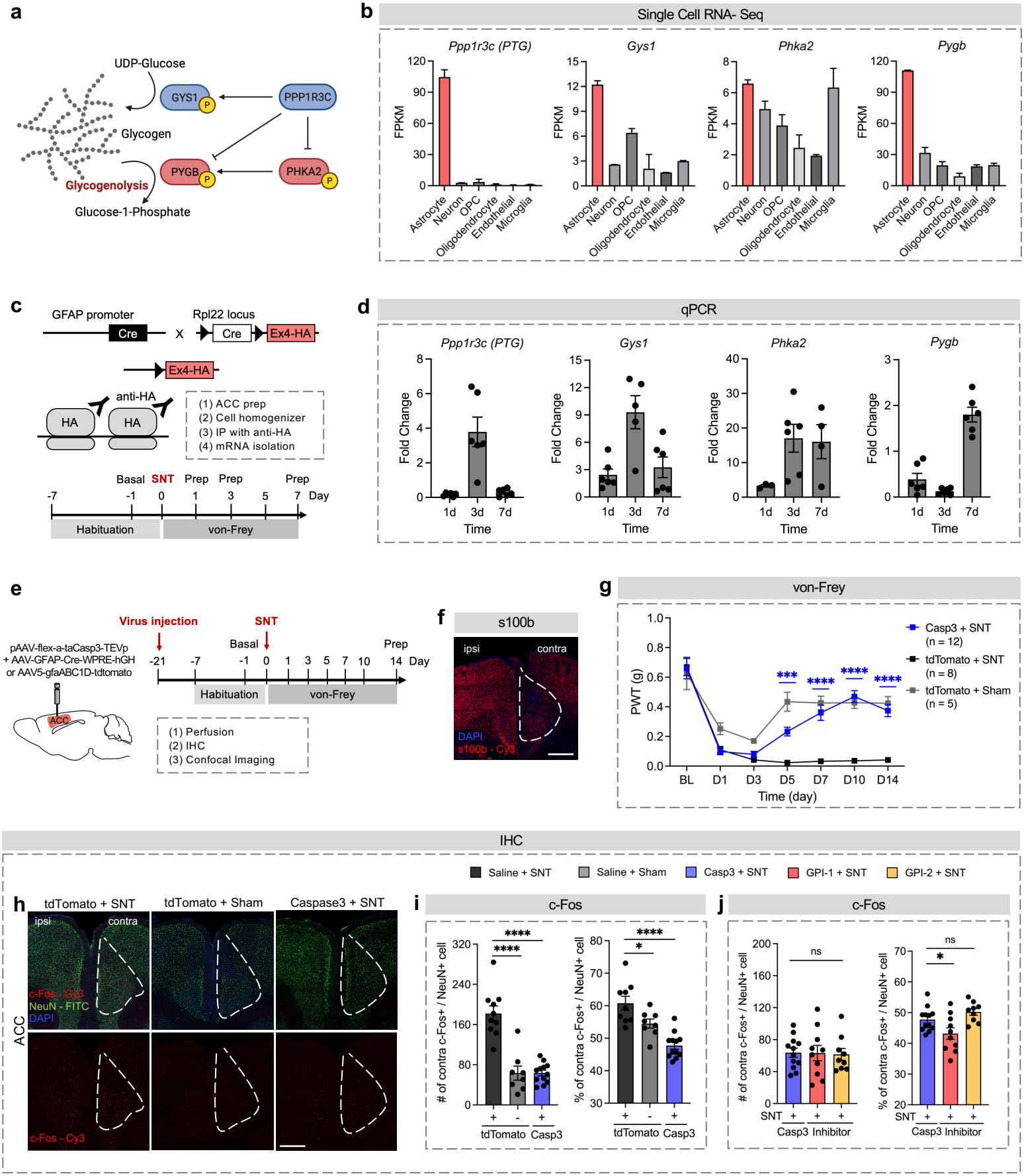

Figure 2. Astrocyte-specific mechanisms underlie altered glycogen dynamics and pain chronification.

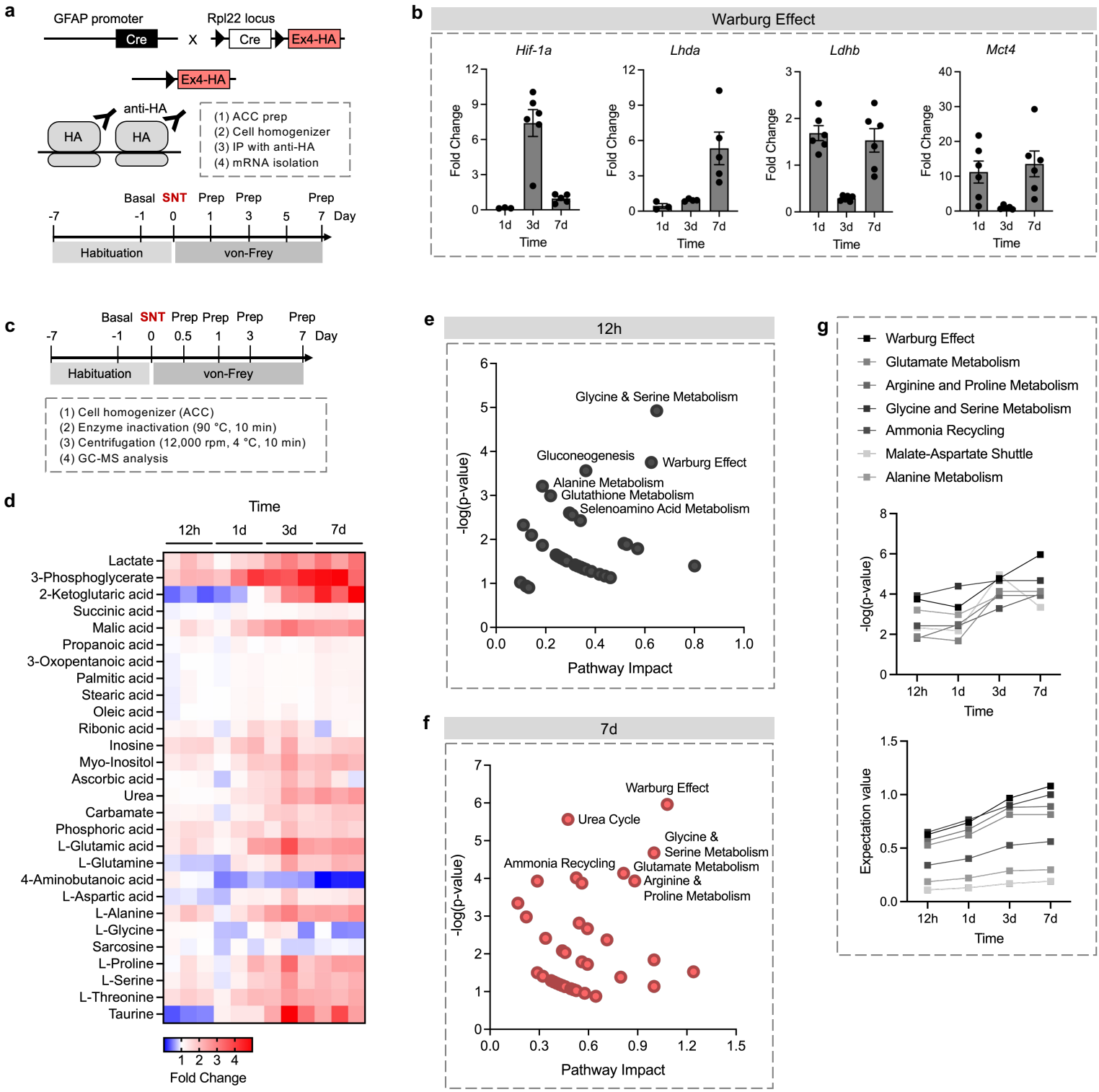

Figure 3. Identification of ACC metabolic dynamics during neuropathic pain chronification.

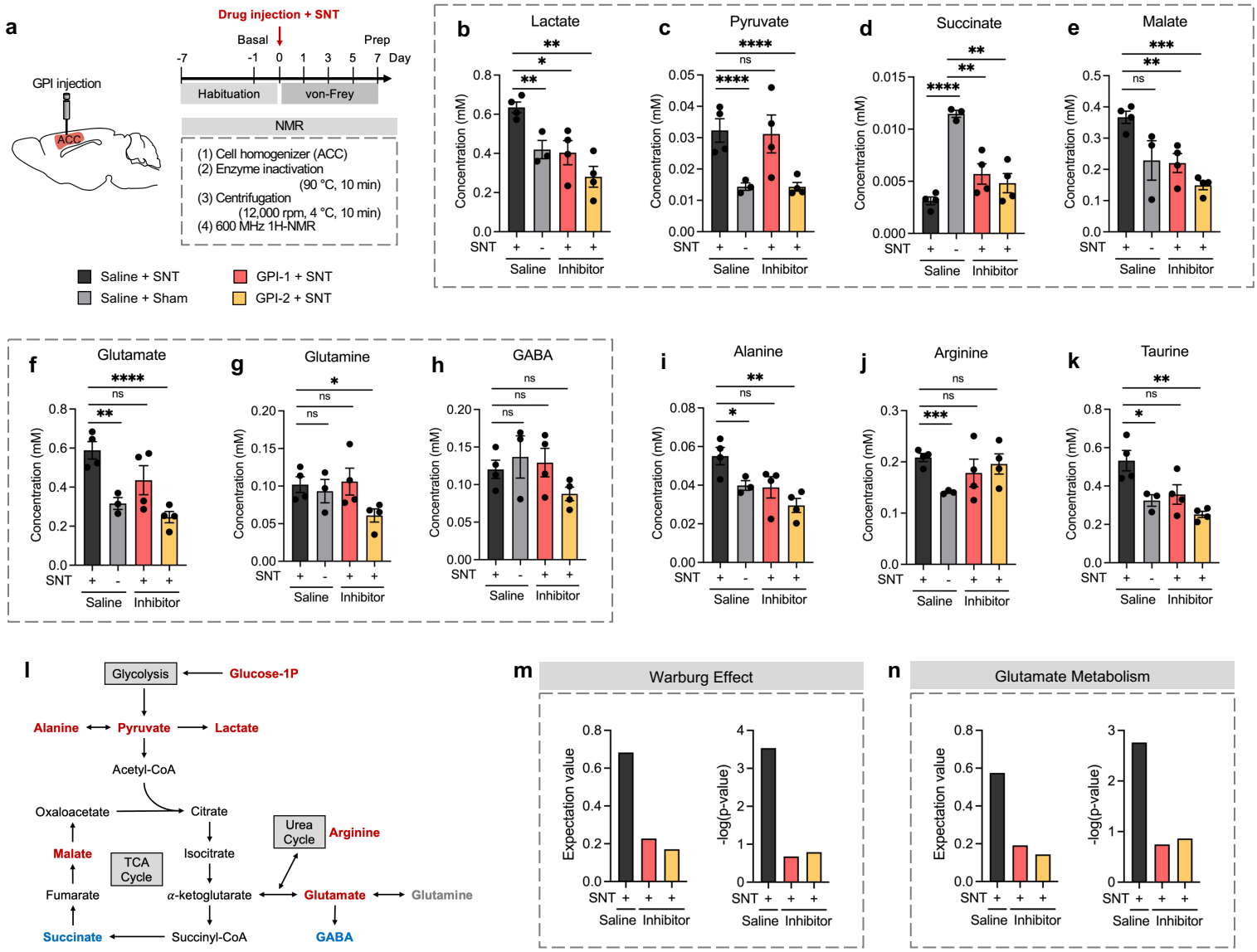

Figure 4. ACC glycogenolysis mediates cancer-associated metabolic changes in neuropathic pain chronification.